

# Aggregating ability of ferric chloride in the presence of phosphate ligand

B. Lartiges <sup>a,\*</sup>, A.G. El Samrani <sup>b,\*\*</sup>, E. Montargès-Pelletier <sup>c</sup>, I. Bihannic <sup>c</sup>, V. Briois <sup>d</sup>, L. Michot <sup>e</sup>

<sup>a</sup> University of Toulouse (Paul Sabatier), Geosciences Environment Toulouse (UMR CNRS-UPS 5563 IRD 234), 14 Av. E. Belin, 31400, Toulouse, France

<sup>b</sup> Lebanese University, Platform for Research and Analysis in Environmental Sciences, Doctoral School of Science and Technology, Faculty of Sciences, P.O. Box. 5, Campus Rafic Hariri, Beirut, Lebanon

<sup>c</sup> University of Lorraine, LIEC (Laboratoire Interdisciplinaire des Environnements Continentaux), UMR CNRS 7360, 54501, Vandoeuvre-les-Nancy, France

<sup>d</sup> SOLEIL Synchrotron, UR1-CNRS, l'Orme des Merisiers, BP 48, Saint-Aubin, 91192, Gif-sur-Yvette, France

<sup>e</sup> Laboratoire PHENIX CNRS Sorbonne Université UMR 8234, 4 Place Jussieu, 72522, Paris Cedex 5, France

## ARTICLE INFO

### Article history:

Received 22 April 2019

Received in revised form

2 August 2019

Accepted 6 August 2019

Available online 6 August 2019

### Keywords:

Coagulant species

Coagulation

Aggregation

Phosphate anions

EXAFS

Ferric chloride

## ABSTRACT

Complexing anions such as phosphate or silicate play an ambivalent role in the performance of hydrolyzing metal coagulants: On one hand, they significantly interfere with the hydrolytic pathway of conventional iron or aluminum coagulants, the associated destabilization mechanism remaining rather elusive; on the other hand, they have been shown to be key ingredients in the formulation of innovative coagulant solutions exhibiting improved removal efficiency, their action mechanism at the molecular scale being presently poorly understood. In this paper, we explore the effect of small additions of phosphate ligand on the chemical coagulation of silica nanoparticles with ferric chloride. Transmission Electron Microscopy-Energy Dispersed X-ray Spectroscopy (TEM-EDXS) combined with Extended X-ray absorption Fine Structure Spectroscopy (EXAFS) at the Fe K-edge are used to provide an insight into the nature of coagulant species, whereas jar-tests, laser diffraction, Small Angle X-ray Scattering (SAXS), and electrophoretic mobility, are used to investigate the aggregation dynamics of silica particles in the presence of phosphate ligand. We show that, in spite of a slight increase in the consumption of iron coagulant, the addition of phosphate significantly improves the formation of silica aggregates provided that the elemental Fe/P ratio remains above 7. Such effects originate from both a large increase in the overall number of coagulant species, the binding of a phosphate ligand terminating the growth of polymeric chains of edge-sharing Fe octahedra, and a change in the nature of the coagulant species that evolves with the Fe/P ratio, small polycations built-up from Fe-oligomers linked by phosphate tetrahedra being eventually formed. Those non-equilibrium nanosize Fe–P coagulant species assemble the silica nanoparticles to form hetero-aggregates whose structure is consistent with a Diffusion-Limited Cluster Aggregation mechanism.

© 2019 Elsevier Ltd. All rights reserved.

## 1. Introduction

Identifying the exact aggregation mechanisms when using aluminum or iron-based coagulants is crucial in drinking water and wastewater treatment operations. Until now, the classical destabilization mechanisms reported in the literature, *i.e.* charge

neutralization with iron or aluminum hydrolysis products in the acidic pH range and enmeshment within an abundant mass of amorphous precipitate at basic pH (Duan and Gregory, 2003; Yu et al., 2015), have not been clearly linked to usual aggregation descriptors such as floc size or floc growth rate. As a result, day-to-day operations, such as readjusting the optimal coagulant concentration following a change in raw water quality, remain mainly based on empirical guidelines (El Samrani et al., 2008). The primary reason for such limitations originates from the complex interplay between the various physico-chemical parameters that underlie coagulation of raw water: when added to water, the iron or

\* Correspondence author.

\*\* Corresponding author.

E-mail addresses: [bruno.lartiges@get.omp.eu](mailto:bruno.lartiges@get.omp.eu) (B. Lartiges), [antoineelsamrani@ul.edu.lb](mailto:antoineelsamrani@ul.edu.lb) (A.G. El Samrani).

aluminum salt hydrolyses to yield hydrolysis products; this lowers the pH of the treated water, which subsequently modifies the charge of the colloidal matter and the organization of the natural organic matter during the course of aggregation (Sieliechi et al., 2008; Chen et al., 2018). In addition, the presence of complexing anions may significantly alter the hydrolytic pathway of the coagulant (Rose et al., 1996, 1997; Vilg -Ritter et al., 1999; Doelsch et al., 2000, 2003), and hence the nature of hydrolysis products responsible for aggregation (El samrani et al., 2004, 2006). Preformed coagulant species such as  $Al_{13}$  polycations have also been shown to depolymerize upon association with colloidal matter present in the raw water (Lartiges et al., 1997; Masion et al., 2000).

This paper attempts to decipher the intricate relationships between simple aggregation descriptors and the nature of coagulant species formed in the particular case of silica nanoparticles aggregated with ferric chloride in the presence of phosphate ligands at pH 7.5. Ferric chloride is a hydrolyzing metal salt commonly used in drinking water treatment for turbidity removal and in wastewater treatment for phosphate elimination (Sieliechi et al., 2008; Hauduc et al., 2015). In view of the selected pH and range of phosphate concentrations the present study is more relevant to wastewater treatment than drinking water treatment (El samrani et al., 2004; Houhou et al., 2009). However, our investigation may also open new lines of research on the synthesis of innovative inorganic coagulants, enhanced aggregation efficiency being observed with iron-based coagulants prepolymerized in the presence of  $PO_4^{3-}$  and  $SiO_4^{4-}$  ligands (Wang et al., 2000; Chen et al., 2015).

The aggregation of silica nanoparticles was followed by turbidity removal, electrophoretic mobility of aggregates, kinetics of floc growth and maximum floc size reached during aggregation using laser diffraction, and floc structure at the semi-local scale using SAXS. The nature of Fe–P hydrolysis products was investigated by EXAFS at the Fe K-edge combined with TEM-EDXS. EXAFS probes the average local atomic environment around the Fe atoms and provides the numbers, types, and interatomic distances to neighboring atoms, whereas TEM-EDXS enables the determination of average Fe/P elemental ratio of aggregates. We show that, even though the presence of phosphate complexing ligand involves a slight additional consumption in coagulant, floc growth and turbidity removal can be optimized with an appropriate addition of phosphate ligand.

## 2. Experimental section

### 2.1. Sample preparation

The suspensions of silica nanoparticles were prepared from the dilution of Ludox HS40 colloidal silica (Sigma-Aldrich) to 500 mg/L using a  $4 \times 10^{-3}$  mol/L  $NaHCO_3$  solution to provide an ionic strength buffer (Lartiges et al., 1997). Ludox HS40 silica nanoparticles are almost spherical in shape with an average diameter of 14 nm (Axelos et al., 1989). An aliquot of phosphate solution taken from a 0.1 mol/L  $Na_2HPO_4 \cdot 2H_2O$  stock solution was then added to the silica suspension before adjusting the pH of the suspension to 7.5 by dropwise addition of dilute HCl.

A commercial unhydrolyzed ferric chloride solution (Arkema), 38 % wt in  $FeCl_3$  and 1.4 in density, was used as coagulant. The aggregation experiments were conducted in a 1L reactor equipped with 4 plexiglas baffles and a rectangular paddle placed at one-third of the reactor height from the bottom (Lartiges et al., 1997). The coagulant was added under agitation as a pure solution with a micropipette (Eppendorf) and stirring was maintained at 100 rpm (average velocity gradient  $G$  of  $135 \text{ s}^{-1}$ ) for 40 min. The coagulated suspension was then allowed to settle for 24h in graduated Imhoff cones. Such settling time is unusually long for a jar-test but is

required to compare, for a given amount of added phosphate, the settling of aggregates formed in the presence and in the absence of silica nanoparticles. It is also worth noting that the drop in pH after ferric chloride addition was less than 1 in the range of coagulant concentrations investigated.

### 2.2. Aggregates characterization

After 24h of settling, 50 mL of supernatant were collected from about 25 mm below the free surface with a syringe. The residual turbidity of supernatant was measured with a Hach XR ratio turbidimeter, and 30 mL of supernatant were filtered on a  $0.2 \mu\text{m}$  pore size cellulose acetate membrane (Machery-Nagel) for analysis of dissolved Fe, Si and P (ICP-AES - Jobin-Yvon 70 type B model).

The electrophoretic mobility of aggregates was determined using a Zetaphoremeter III (Seph/CAD) equipped with a CCD camera to track the trajectories of aggregates under a constant direct-current electric field ( $800 \text{ V/m}$ ). 1 mL of settled sediment was re-dispersed in the corresponding supernatant before being pumped to the measurement cell. About 100 measurements of aggregate mobility were carried out for a given coagulant/phosphate concentration.

The size distribution of aggregates was measured on-line using a laser diffraction particle size analyzer (Malvern Mastersizer) in the  $1.2\text{--}600 \mu\text{m}$  size range. The aggregated suspension was continuously withdrawn from the bottom of the reactor, passed through the analyzer beam with a peristaltic pump located downstream the measurement cell (flow rate of  $55 \text{ mL/min}$ ), before being recycled to the reactor. Previous experiments, conducted with shear-sensitive aggregates under similar operating conditions, showed that the relative variations in aggregate size measured by the laser sizer were closely related to the changes in agitation conditions inside the reactor rather than to shearing in the transport tubing (Chaignon et al., 2002). Aggregate size measurements were averaged for 1 s and taken every 3 s to ensure a complete renewal of the measurement cell. The volume size distributions thus obtained are monomodal, self-similar during aggregate growth, and hence, the aggregation dynamics can be represented by the temporal evolution of mean aggregate diameter  $D_{50}$ . As already shown in previous studies (Chaignon et al., 2002; Sieliechi et al., 2016),  $D_{50}$  grows linearly with time to reach a maximum diameter  $D_{50\text{max}}$ ; the slope of the straight portion of the curve defines the aggregation rate.

### 2.3. Sediment characterization

Small-angle X-ray scattering (SAXS) experiments were performed using freshly settled aggregates on the D22 beamline at LURE synchrotron facility (Orsay-France). The detector was positioned at 2.52 m from the sample. The collected data covered the  $Q$ -range from  $2.5 \times 10^{-3}$  to  $10^{-1} \text{ \AA}^{-1}$  with  $Q = 4\pi\sin(\theta)/\lambda$  in which  $Q$  is the magnitude of the scattering vector,  $2\theta$  the scattering angle, and  $\lambda$  the wavelength of X-rays ( $1.49 \text{ \AA}$ ). Such range of  $Q$ -values does not cover the Guinier regime of silica aggregates obtained in this study but allows studying the fractal regime below  $1 \mu\text{m}$ . The intensity scattered by the aggregates can be expressed as:  $I(Q) = K I_0(Q) G(Q)$  where  $K$  is a constant,  $I_0(Q)$  the intensity scattered by a single silica particle, and  $G(Q)$  an interference function related to the particle arrangement within the aggregate. When the aggregates are fractal,  $G(Q)$  can be approximated by  $G(Q) \sim Q^{-D_f}$  in the  $[1/L - 1/R_0]$   $Q$  range where  $D_f$  is the fractal dimension of aggregates,  $L$  the characteristic length of aggregates, and  $R_0$  the size of elementary particles (Ramsay and Booth, 1983).

The sediment was freeze-dried before observation with a Philips CM20 Transmission Electron Microscope equipped with an Energy Dispersive X-ray Spectrometer (EDAX). The powder was dispersed

by sonication in ethanol and a drop of suspension was then evaporated on a carbon-coated copper grid. After calibration of the Energy Dispersive X-ray Spectrometer with a Phosphosiderite standard ( $\text{FePO}_4 \cdot \text{H}_2\text{O}$ ), the Fe/P elemental ratio of aggregates was determined from about 50 EDX spectra collected at random locations using a 70 nm probe size and a 30 s counting time acquisition.

EXAFS experiments were performed on the D42 beamline at LURE synchrotron facility. The freeze-dried sediment was prepared as pellets using microcrystalline cellulose. The X-ray absorption spectra were recorded in transmission mode at room temperature around the Fe K-edge from 7000 to 8100 eV with 2 eV steps and 2 s collecting time. EXAFS data reduction was performed according to a standard procedure previously described (Manceau and Calas, 1986). A Kaiser window ( $3.5\text{--}14.7 \text{ \AA}^{-1}$ ) was used for deriving Fourier transforms from EXAFS spectra (Bonnin et al., 1985). The Radial Functions (RDF) thus obtained are not corrected for phase shifts, which leads to peaks shifted down by about  $0.3 \text{ \AA}$  compared with crystallographic distances. Fitting was essentially carried out on the second coordination shell, on the backfiltered  $k^3\chi(k)$  curves in the  $[2.1\text{--}3.5] \text{ \AA}$  range. Theoretical phase and amplitude functions were used to obtain the number of neighbors in the shell around the absorbing Fe atom and the radial distances, as well as the Debye-Waller factors ( $\sigma$ ). The electron mean free path ( $G = k/\lambda$ ) and the energy shift ( $\Delta E$ ) were respectively fixed at  $0.82 \text{ \AA}^{-1}$  and 5 eV.

### 3. Results

#### 3.1. Destabilization of silica nanoparticles with ferric chloride in the presence of phosphate ligand

Typical curves of residual turbidity as a function of ferric chloride concentration in the presence of various amounts of phosphate are shown in Fig. 1a. The curves exhibit similar profiles characteristic of a nanoparticle suspension increasingly aggregated by the addition of coagulant (Sieliechi et al., 2008): at low ferric chloride concentration, the turbidity of the supernatant steadily increases as small non-settleable aggregates of increasing size are formed. After reaching a maximum, the residual turbidity steeply decreases with further coagulant addition when settling aggregates are obtained. A rapid build-up in sediment volume is then observed in that

concentration range (Fig. 1b). The minimum ferric chloride concentration that determines the highest level of turbidity reduction defines the optimal coagulant dose  $[\text{Fe}]_{\text{opt}}$ .

The presence of phosphate ligand has two main effects: (i) the maximal residual turbidity is lowered upon addition of low P levels and then increases with further addition of P; (ii) the residual turbidity curve is stretched towards higher coagulant concentrations, or in other terms, the addition of P to the silica suspension increases  $[\text{Fe}]_{\text{opt}}$ . Actually, as illustrated in Fig. 2a,  $[\text{Fe}]_{\text{opt}}$  becomes proportional to the phosphate content of the suspension above a P concentration of  $0.5 \text{ mmol/L}$ , i.e. a Fe/P molar ratio less than 2, regardless of silica concentration. As the removal of P and silica nanoparticles occurs simultaneously when settleable aggregates are formed (Fig. 2b), it is clear that all the components – silica nanoparticles, phosphate, and iron coagulant – participate together in the aggregation process.

To further investigate the aggregation behavior of silica nanoparticles at low phosphate concentrations, a series of experiments were conducted with increasing phosphate concentrations and a fixed amount of ferric chloride (Fig. 3). The coagulant concentration selected ( $0.36 \text{ mmol/L}$ , i.e. close to the maximum of residual turbidity in the absence of phosphate ligand – see Fig. 1a) helps exacerbating the sensitivity to phosphate additions; further underdosing, or on the contrary iron concentrations in the optimal dosing range, would reduce the range of turbidity variation. For an iron concentration equal to  $0.36 \text{ mmol/L}$ , the addition of small amounts of phosphate ligand linearly decreases the level of residual turbidity from an initial high level of about 27 NTU to reach a minimum of 12 NTU for a Fe/P molar ratio of about 7, before slightly re-increasing; on the other hand, the sediment volume increases and reaches a maximum that is slightly shifted to higher Fe/P ratios (i.e. lower phosphate concentrations) before returning to zero (Fig. 3). According to Fig. 1a, it can be expected that the residual turbidity will decrease again at higher phosphate concentration.

#### 3.2. Characterization of aggregates

That a small addition of phosphate ligand improves the removal of silica nanoparticles with ferric chloride implies a significant change of aggregate properties. Fig. 4a shows typical temporal evolutions of the mean aggregate diameter  $D_{50}$  for various added P

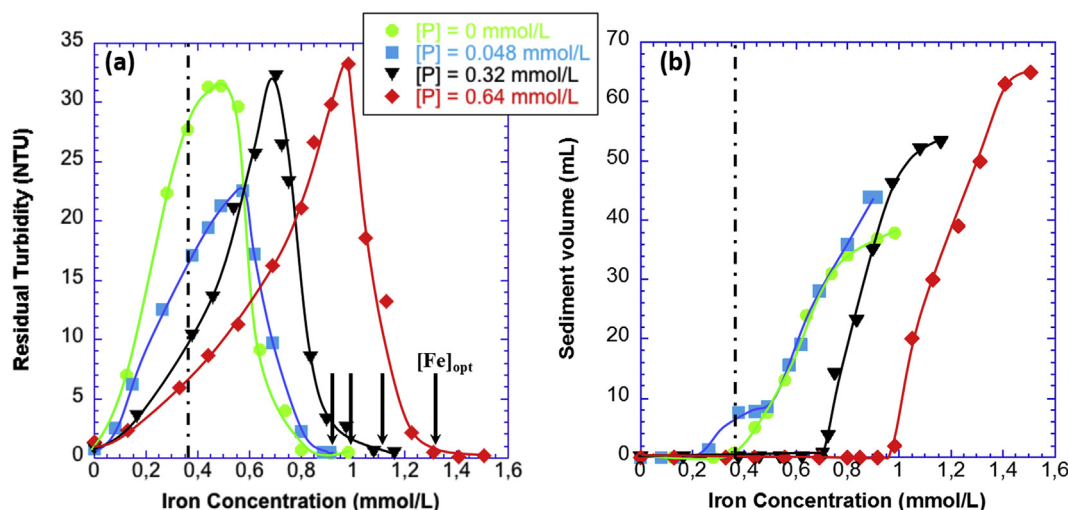


**Fig. 1.** Jar-test results for a 500 mg/L suspension of silica particles in the presence of various phosphate ligand additions. (a) Residual turbidity as a function of iron concentration. (b) Sediment volume as a function of iron concentration. The hyphenated lines indicate the  $0.36 \text{ mmol/L}$  iron coagulant concentration. The arrows show the optimum coagulant concentrations. The error bars are smaller than the size of the symbols.

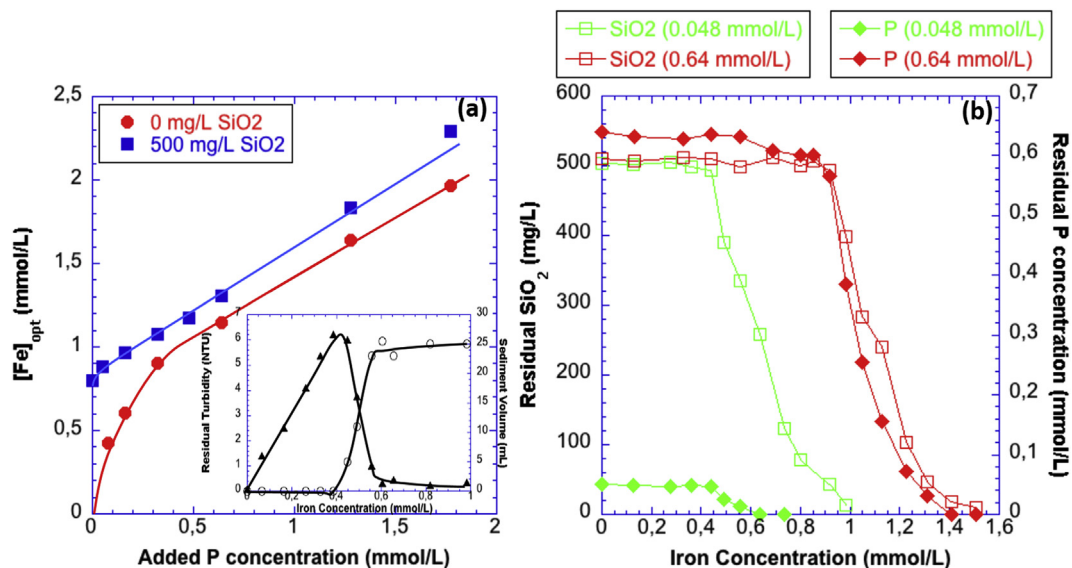


**Fig. 2.** (a) Optimum iron coagulant dose as a function of phosphate addition, (●) without silica particles in suspension, (■) with a 500 mg/L silica suspension. The inset shows the jar-test results for a 0.32 mmol/L P concentration coagulated with the iron coagulant in the absence of silica nanoparticles. The other jar-test results are given in figure S1 of Supporting Information. (b) Residual concentrations in phosphorus (◆) and SiO<sub>2</sub> (□) as a function of iron concentration for suspensions of 500 mg/L SiO<sub>2</sub> and initial phosphorus additions of 0.048 mmol/L and 0.64 mmol/L.

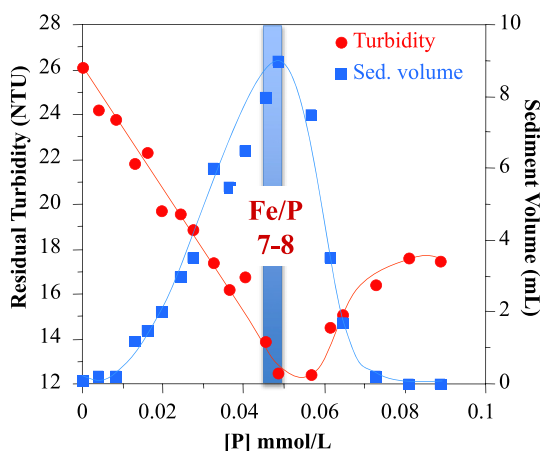


**Fig. 3.** Evolution of Residual turbidity (●) and sediment volume (■) as a function of phosphate addition for an iron coagulant concentration of 0.36 mmol/L. The thick bar in blue indicates the [7–8] range in Fe/P. (For interpretation of the references to colour in this figure legend, the reader is referred to the Web version of this article.)

concentrations and an iron coagulant concentration of 0.36 mmol/L. Both the aggregation rate and the maximum mean aggregate diameter are inferred from these curves. Fig. 4b presents the corresponding evolution of aggregation rate and maximum mean aggregate diameter ( $D_{50max}$ ) with phosphate concentration. Like residual turbidity and sediment volume, both the aggregation rate and the  $D_{50max}$  drastically vary with small phosphate additions: the aggregation rate steeply increases from initially non-measurable values to reach a 50  $\mu\text{m}/\text{min}$  growth at a Fe/P molar ratio of about 14 and then gradually returns to zero;  $D_{50max}$  also increases from an initial value lower than the measuring range of the particle sizer to reach a maximum mean aggregate diameter of about 110  $\mu\text{m}$  at a Fe/P ratio of 7, and then drops to submicron sizes at higher phosphate concentrations.

An elemental ratio Fe/P in the [7–8] range is also a threshold value for the structure of aggregates. The SAXS curves, shown in

Fig. 5a as a Log-Log plot of the scattering intensity versus the scattering vector, are characterized by a linear portion that identifies the fractal region in the  $[6 \cdot 10^{-3} - 4 \cdot 10^{-2} \text{ \AA}^{-1}]$  Q range, followed by a cross-over at higher Q that corresponds to the scattering of silica nanoparticles of radius 7 nm. The fractal dimension  $D_f$  obtained from the slope of the scattering factor remains close to 1.72 for small additions of phosphate ligand (Fig. 5b). However, above a Fe/P of 7,  $D_f$  exhibits a step increase to an average value of 1.83. On the other hand, the electrophoretic mobility of aggregates, varying between  $-2.95$  and  $-3.05 \mu\text{m s}^{-1}/\text{V.cm}^{-1}$ , remains almost constant in the range of P concentration investigated (Fig. 6). The diameter of Ludox silica nanoparticles (14 nm) is well below the lower size limit of particles (about 0.2  $\mu\text{m}$ ) that can be followed from the image analysis system of a Zetaphoremeter III. However, it is expected that the electrophoretic mobility of pristine silica particles is lower than  $-3 \mu\text{m s}^{-1}/\text{V.cm}^{-1}$  since such value was reported for Ludox HS particles in a suspension of same ionic strength as ours but at pH 6 (Fatombi et al., 2013).

### 3.3. Nature of coagulant species

EDX microanalysis provides a first approach to the nature of hydrolysis products that trigger the aggregation of silica nanoparticles (Fig. 7). The histograms of Fe/P atomic ratios measured on the freeze-dried sediments obtained for a given ferric chloride concentration and increasing phosphate concentrations reveal that, at low phosphate concentration, i.e.  $\text{Fe/P} \geq 10$ , the Fe/P atomic ratios are rather uniformly distributed across the 2–10 range. At higher phosphate concentrations, i.e.  $(\text{Fe/P} \leq 8)$ , the width of Fe/P distributions becomes narrower and a maximum around 4–5 clearly emerges. This suggests that well-defined coagulant species, formed from the complexation of hydrolyzed Fe and phosphate ligands, are developing with increasing phosphate concentration.

EXAFS curves and  $k^3$ -weighted Fourier transforms of EXAFS oscillations into R-space are reported in Fig. 8. The first peak of the Fourier transform, or radial distribution function RDF, is centered at 1.5  $\text{\AA}$  and represents the first coordination shell around iron atoms. This first shell is composed of 6 oxygen atoms with a Fe–O bond



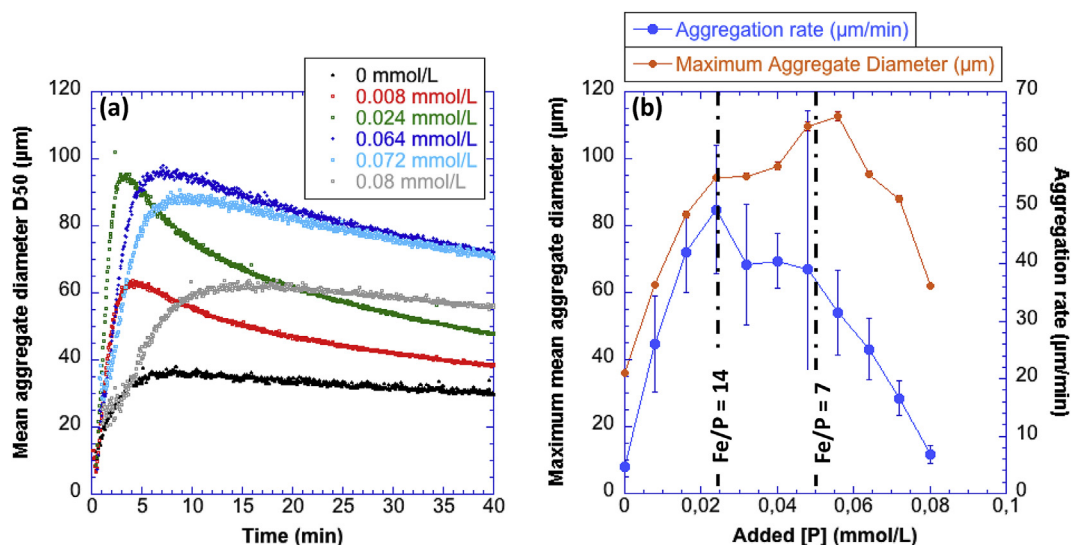


**Fig. 4.** (a) Temporal evolution of mean aggregate diameter (D50) for various added P concentrations and an iron coagulant concentration of 0.36 mmol/L. (b) Evolution of aggregation rate (●) and maximum aggregate size (●) as a function of phosphate concentration for an iron coagulant concentration of 0.36 mmol/L. The confidence intervals for the aggregation rate were obtained using a Student t-test with a significance level of 5%. The standard deviation for the maximum mean aggregate diameter was calculated from the variation of diameter in the vicinity of the maximum of the D<sub>50</sub> vs time curve.

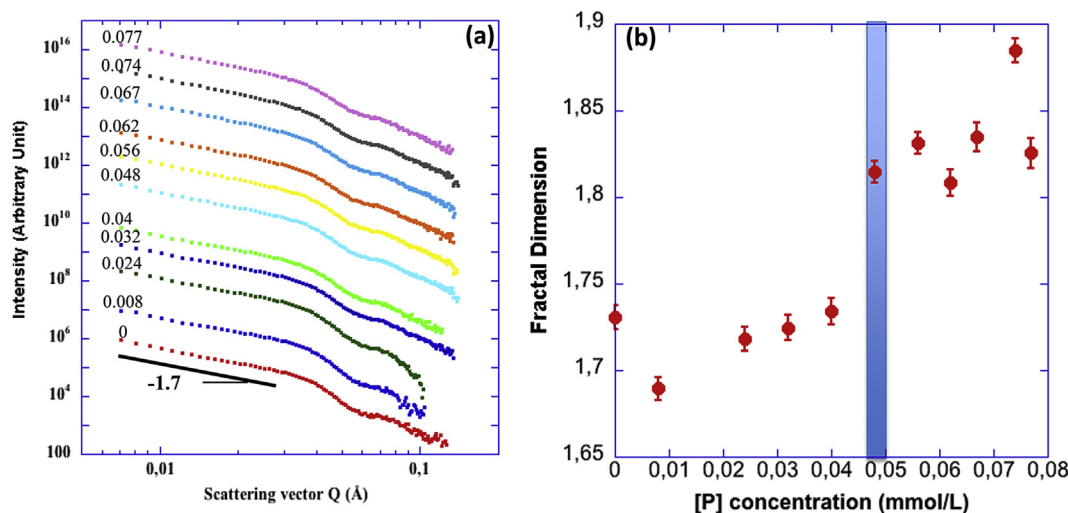


**Fig. 5.** (a) Log-Log plot of scattering intensity versus scattering vector for sediments obtained with an iron coagulant concentration of 0.36 mmol/L and various phosphate concentrations (mmol/L) indicated on the left of the SAXS curve. (b) Evolution of the fractal dimension (inferred from the slope of the linear portion of the SAXS curves in (a)) as a function of phosphate concentration. The thick bar in blue indicates the [7–8] range in Fe/P. The confidence intervals for the slope of the regression line giving the fractal dimension were calculated using a Student t-test with a significance level of 5%.

length close to 2 Å, which is consistent with previous X-ray absorption studies (Bottero et al., 1994; Zhu et al., 2013; Collins et al., 2016). The second peak, centered at 2.7–2.8 Å, is of greater interest since it reflects the average degree of iron polymerization. In our case, three kinds of atoms, Fe, P, and Si, can be expected in the second coordination shell of iron atom.  $K^3\chi(k)$  curves reveal a small oscillation centered at  $7.5 \text{ \AA}^{-1}$  typical of heavy atoms, and hence a Fe contribution in the second shell, that sharply decreases with increasing phosphate concentration. In parallel, the intensity of the second peak of the Fourier Transform gradually decreases.

The fitting results are reported in Table 1 and Fig. 9. In the absence of phosphate addition, i.e. P/Fe = 0, two iron neighbors sub-shells are necessary for fitting. The distances thus obtained, 3.04 and 3.14 Å, identify edge-sharing Fe–O octahedra (Bottero et al., 1994; Doelsch et al., 2000; Collins et al., 2016). The fitting

can be slightly improved by the addition of a third shell assigned to a Fe–Si contribution. Si being a lighter atom in comparison with Fe, its contribution as a backscatterer in the EXAFS oscillations can be argued. In particular, the number of Si neighbors is rather inaccurate.

Upon the addition of [P] = 0.008 mmol/L to the silica suspension, i.e. Fe/P = 45, the EXAFS curve is fitted with two sub-shells of Fe–Fe edge-sharing bonding and a supplementary shell of iron atoms linked by double corner sharing (Fig. 10B). Further increase in phosphate significantly decreases the number of iron neighbors sharing edges from  $2.5 (\pm 0.5)$  to  $1.5 (\pm 0.5)$  ( $N_1 + N_2$  in Table 1), the Fe–Fe distance varying from 2.98 to 3.04 Å ( $\pm 0.1 \text{ \AA}$ ) for the first sub-shell and from 3.13 to 3.15 Å ( $\pm 0.1 \text{ \AA}$ ) for the second sub-shell. The contribution of double corner sharing Fe–Fe bonding could not be evidenced, which implies a limited hydrolysis of iron species.

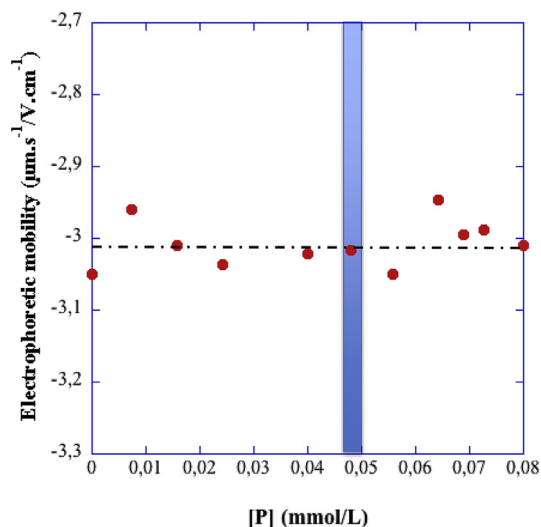


**Fig. 6.** Evolution of the aggregate electrophoretic mobility as a function of phosphate addition for an iron coagulant concentration of 0.36 mmol/L. The thick bar in blue indicates the [7–8] range in Fe/P.

Above a P addition of 0.008 mmol/L, the curve fitting is mainly performed using edge-sharing Fe–Fe bonding, corner-sharing Fe–P bonding, and in the case of Fe/P = 6.4 and Fe/P = 5.8, with corner-sharing Fe–Fe bonding. The values of Fe–Fe bond length (3.56 and 3.58 Å respectively for Fe/P = 6.4 and Fe/P = 5.8) may identify the presence of double corner-sharing trimers (Fig. 10B) or Fe<sub>2</sub>P complexes (Fig. 10E). Actually, the latter geometry should be favored, as phosphate neighbors are needed for an appropriate fitting.

The structural parameters inferred from curve-fitting analysis reveal that the presence of phosphate ligand decreases the number of iron neighbors, i.e. a decrease of Fe–Fe bonds, and leads to a contribution of phosphorus atoms in the second coordination shell of Fe. The number of phosphate neighbors is highly variable from one sample to another, but it should be noted that those numbers are rather inaccurate and are only given to evidence the presence of

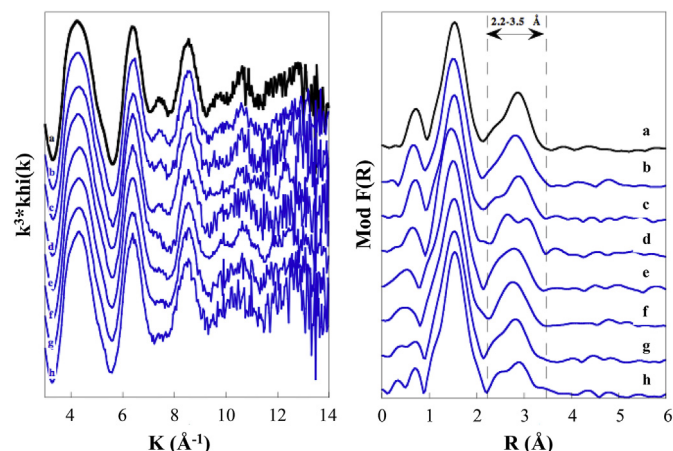


**Fig. 8.** EXAFS oscillations ( $k^3 \cdot \chi(k)$ ) and Fourier Transform curves calculated in the [3.7–13] Å<sup>−1</sup> range with a Kaiser window,  $t = 3$ ; a: P/Fe = 0; b: Fe/P = 45 (0.008 mmol/L in P); c: Fe/P = 18 (0.02 mmol/L in P); d: Fe/P = 15 (0.024 mmol/L in P); e: Fe/P = 9 (0.04 mmol/L in P); f: Fe/P = 7.5 (0.048 mmol/L in P); g: Fe/P = 6 (0.06 mmol/L in P); h: Fe/P = 5 (0.072 mmol/L in P).

Fe–P bonds. In contrast, the values of Fe–P bond length, between 3.26 and 3.34 Å, are unambiguously assigned to the formation of single-corner sharing complexes (see Fig. 10D, E and F). For Fe/P ratios lower than 18, the phosphate ligand substitution for Fe does not prevent the formation of Fe-dimers and Fe-trimers, the number of neighbors (subshells 1 and 2) remaining above 1. Nevertheless, the presence of phosphate certainly changes the size of iron polymer chains, but, as the curve fitting was performed in the [2.5–3.8] Å distance range, no information can be inferred about the chain size and the semi-local structure of iron octahedra aggregates.

## 4. Discussion

### 4.1. Nature of coagulant species in the system ferric chloride/phosphate/silica nanoparticles

Most of the information available in the literature on iron (III)

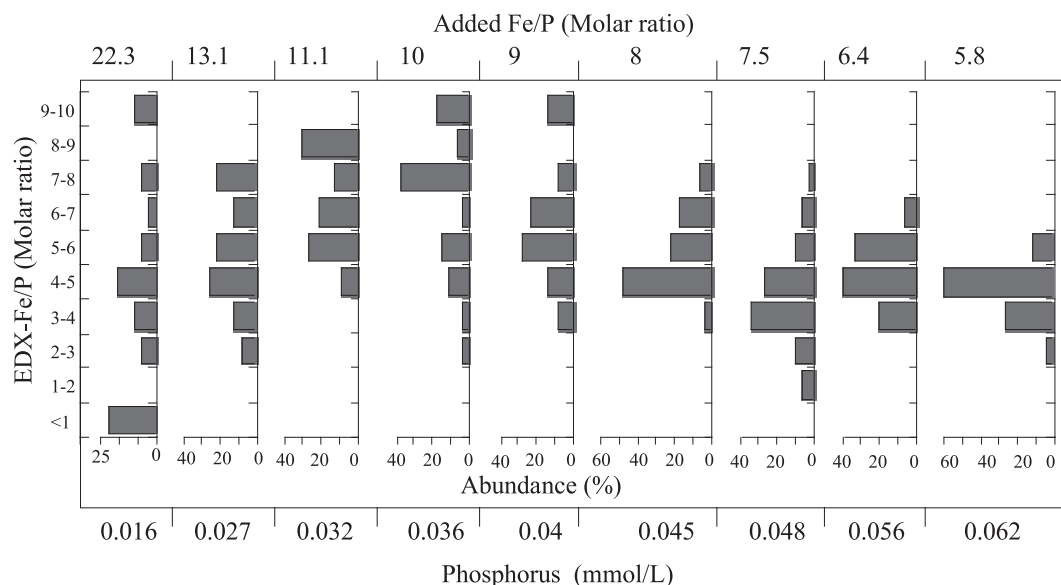


**Fig. 7.** Frequency histograms of Fe/P elemental ratio obtained from TEM-EDXS microanalysis on freeze-dried sediments as a function of phosphate concentration for an iron coagulant concentration of 0.36 mmol/L.

**Table 1**

Fitting results. Ni number of neighbors constituting the i shell. R: bond length (Å).  $\sigma$ : Debye Waller factor (Å). Energy shift was fixed to 5 eV and mean free path related factor,  $\Gamma$ , was fixed to 0.82 Å<sup>-2</sup>.

Sample	N1 Fe–Fe	R1	$\sigma$ 1	N2 Fe–Fe	R2	$\sigma$ 2	N3 Fe–P or Fe–Si	R3	$\sigma$ 3	N4 Fe–Fe	R4	$\sigma$ 4
P/Fe = 0	1.2	3.0	0.08	1.3	3.14	0.07	1.0	3.28	0.100			
Fe/P = 45	1.4	3.04	0.100	0.9	3.15	0.09	0.9	3.28	0.1	0.7	3.46	0.09
Fe/P = 18	0.9	2.99	0.08	1	3.14	0.07	0.9	3.29	0.08	–	–	–
Fe/P = 15	0.9	3.04	0.06	0.7	3.20	0.06	1.0	3.28	0.06			
Fe/P = 9	0.8	2.99	0.06	0.9	3.13	0.06	0.8	3.328	0.1			
Fe/P = 7.5	0.6	3.03	0.06	0.7	3.15	0.06	1.2	3.29	0.11			
Fe/P = 6.4	0.8	3.01	0.07	0.8	3.14	0.06	0.6	3.34	0.1	0.6	3.58	0.07
Fe/P = 5.8	0.7	2.98	0.06	0.8	3.13	0.06	0.4	3.26	0.06	0.9	3.56	0.06

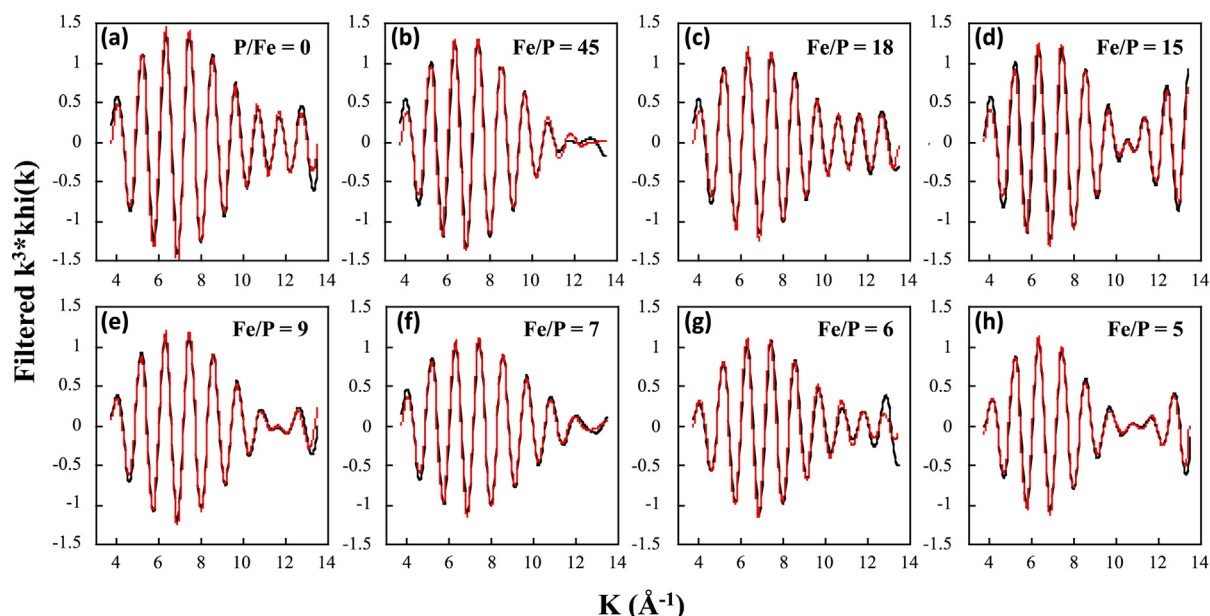


**Fig. 9.** Experimental and theoretical (dashed line) back filtered  $k^3 \cdot \chi(k)$  curves corresponding to 2nd coordination shell [2.2–3.5] Å. (a) P/Fe = 0; (b) Fe/P = 45 (0.008 mmol/L P); (c) Fe/P = 18 (0.02 mmol/L P); (d) Fe/P = 15 (0.024 mmol/L P); (e) Fe/P = 9 (0.04 mmol/L P); (f) Fe/P = 7.5 (0.048 mmol/L P); (g) Fe/P = 6 (0.06 mmol/L P); (h) Fe/P = 5 (0.072 mmol/L P).

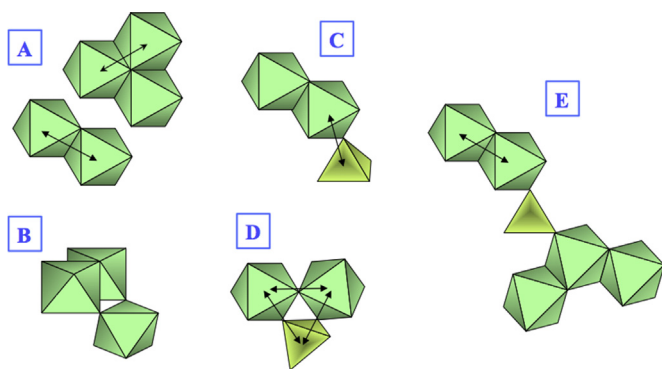


**Fig. 10.** Possible local structures of Fe–P coagulant species: (A) Edge-sharing dimer or trimer, distance [Fe–Fe] ~ 3.0–3.2 Å. (B) Double corner-sharing trimer, distance [Fe–Fe] ~ 3.45–3.55 Å. (C) Single corner sharing with a SiO<sub>4</sub> or PO<sub>4</sub> tetrahedron, distance [Fe–P] ~ 3.0–3.3 Å. (D) Single corner sharing Fe complex, distance [Fe–Fe] ~ 3.4–3.6 Å. (E) Fe–P oligomeric species.

hydrolysis has been acquired in the context of solutions of high Fe concentration (decimolar to molar) slowly hydrolyzed from acidic conditions (Tchoubar et al., 1991; Bottero et al., 1994; Rose et al., 1996, 1997; Doelsch et al., 2000, 2003; Collins et al., 2016). Thus,

depending on the hydrolysis ratio OH/Fe, dilution and ageing, the hydrolysis of ferric chloride solutions typically yields monomers, corner-sharing dimers, edge-sharing dimers, double-corner trimers, polycations and aggregates of those polycations, that eventually form akaganeite ( $\beta$ -FeOOH) upon ageing (Murphy et al., 1976; Tchoubar et al., 1991; Manceau and Drits, 1993; Bottero et al., 1994). In the presence of organic or inorganic complexing ligands, the speciation diagrams of iron-base solutions are drastically modified. Most often, when a sufficient amount of complexing ligands has been added (e.g. phosphate anions, small organic acids, dissolved organic matter), the hydrolysis of ferric chloride is hindered to the dimer stage (Rose et al., 1996, 1997; Vilg -Ritter et al., 1999; Doelsch et al., 2000). In the case of silicate and sulfate ligands, EXAFS at the Fe K-edge and SAXS experiments revealed the presence of edge- and corner-sharing Fe shells that led to the formation of three-dimensional molecular clusters (Doelsch et al. 2000, 2003; Zhu et al., 2012; Collins et al., 2016).

In contrast, natural raw waters and wastewaters relevant to this study generally show neutral or slightly alkaline pH conditions before being treated with ferric chloride concentrations in the millimolar range or less (El samrani et al., 2004; Caravelli et al., 2010). The rapid hydrolysis of ferric chloride that results from such conditions (Pham et al., 2006) modifies the classical polymerization pathway. In particular, the formation of the double

corner-sharing Fe trimer (Fig. 10B) can only be evidenced for a Fe/P ratio of 45. Instead, polymeric chains of edge-sharing Fe octahedra, equivalent to those obtained from molecular dynamics simulations (Zhang et al., 2015) occur in solution.

In the presence of increasing phosphate concentration, the complexation dynamics becomes gradually dominant over the kinetics of iron (III) hydrolysis. The number of iron neighbors sharing edges decreases, which can be interpreted as the termination of the active chains growth whenever a phosphate ligand binds on the end of a Fe polymer chain. An increased number of oligomeric structures, and hence an increased number of coagulant species, is then formed from edge-sharing Fe dimers/trimers/oligomers linked by a phosphate tetrahedra (Fig. 10). Single corner-sharing Fe octahedra, identified at Fe/P ratios of 6.4 and 5.8, may also participate in the bridging of oligomeric Fe–P chains (Rose et al., 1996). Below a Fe/P molar ratio of 7, the excess phosphate binding on iron dimers/trimers should decrease the charge of coagulant species and/or promote the growth of oligomeric structures through phosphate bridging (Fig. 10). Therefore, both the number and efficiency of coagulant species decrease for a Fe/P less than 7. In summary, if the strong affinity of iron (III) for phosphate lowers the degree of polymerization of iron coagulant (Rose et al. 1996, 1997; El samrani et al., 2004), it also increases at first the number of coagulant species and improves the aggregation of silica nanoparticles. Further addition of phosphate ligand ( $\text{Fe/P} \leq 7$ ) becomes detrimental for aggregation.

To evidence a possible effect of silica nanoparticles on the nature of coagulant species is not straightforward. The detection of Si neighbors using EXAFS at the Fe K-edge is rather difficult because of the large difference in atomic number between Si and Fe. Including a Si shell improves the spectral fitting only in the absence of phosphate. It has been shown that the polymerization of iron (III) is inhibited for Fe/Si molar ratios in the 1 to 4 range (Doelsch et al., 2000). In our case, the number of silanol groups per unit surface area of silica that may interact with the Fe hydrolyzed products, is about  $4.6 \text{ nm}^{-2}$  (Zhuravlev, 2000). Using a specific surface area of  $220 \text{ m}^2/\text{g}$  for the Ludox HS nanoparticles, we calculate a Fe/Si molar ratio of 0.42. Actually, both steric hindrance and charge repulsion between the positive coagulant species attached on the surface of silica nanoparticles should further decrease this ratio. Therefore, the effect of the silica surface on iron hydrolysis is expected to be considerably less than that of phosphate ligand, even though the association of polymeric chains of edge-sharing Fe octahedra with the silica nanoparticles may also inhibit the chain growth.

#### 4.2. Aggregation mechanism of silica nanoparticles in the system $\text{FeCl}_3/\text{PO}_4$

It is especially interesting that the nature of hydrolysis products, and hence the type of coagulant species that bind the silica nanoparticles, significantly changes with the relative concentrations of iron coagulant and phosphate ligand. Such feature has not been addressed in previous physicochemical models for phosphorus removal in which only equilibrium species such as  $\text{FeHPO}_4^+$ ,  $\text{FeH}_2\text{PO}_4^{2+}$  or  $\text{Fe}(\text{OH})_3$  have been considered (Smith et al., 2008; Caravelli et al., 2010; Hauduc et al., 2015). Our study reveals that Fe dimers, through the formation of complexes such as  $\text{Fe}_2(\text{HPO}_4)(\text{OH})(\text{H}_2\text{O})_3^{3+}$  and  $\text{Fe}_4(\text{PO}_4)(\text{OH})_2(\text{H}_2\text{O})_7^{16+}$ , play a significant role during phosphate removal, those transient species nevertheless leading to the thermodynamically favored  $\text{Fe}(\text{PO}_4)(\text{H}_2\text{O})_5$  complex at longer times (Lente et al., 2000; Lente and Fabian, 2002). That the ionic background of the raw water may interfere with the hydrolytic pathway of aluminum or iron coagulants is also overlooked in traditional destabilization mechanisms (Duan and Gregory, 2003). Yet, in continental surface waters, the average contents in silica,

sulfate, phosphate and chloride anions (Meybeck and Helmer, 1989) are in sufficient amounts to modify the polymerization of hydrolyzing metal salts (El Samrani et al., 2006).

It is nevertheless rather difficult to precisely elucidate, for a given Fe/P ratio, both the number and various types of coagulant species. EXAFS and even more TEM-EDXS, only provide an average description of the hydrolysis products present in the bulk solution. If iron oligomers linked by a phosphate tetrahedron may lead to polycations such as  $\text{Fe}_4(\text{PO}_4)(\text{OH})_2(\text{H}_2\text{O})_7^{16+}$ , those highly charged species do not account by themselves for the destabilization of silica nanoparticles. Under the conditions of pH and ionic strength used in this study, the surface charge density of Ludox nanoparticles is about  $-1.6 \mu\text{C}/\text{cm}^2$  (Bolt, 1957; Allison, 2009). This corresponds to 61 negatively charged  $-\text{SiO}^-$  groups per silica particle. In that case, the number of polycations of charge 7 + necessary to neutralize the silica surface would be less than 10. As a 500 mg/L Ludox HS suspension corresponds to a  $1.58 \cdot 10^{17}$  particles per liter, a Fe concentration of  $9.4 \mu\text{mol}/\text{L}$  should then be theoretically sufficient to achieve the neutralization of silica nanoparticles. The latter concentration is two orders of magnitude less than the actual coagulant concentration used. Therefore, the coagulant species present in suspension are certainly a mix of weakly positive hydrolyzed products comprising on the average about 4–5 Fe atoms for one P atom.

As the SAXS curves do not reveal any increase in the radius of elementary particles with P addition, the size of coagulant species is expected to remain in the lower nanometer range. In that context, a sweep-flocculation mechanism, characterized by the formation of an abundant precipitate enmeshing the silica nanoparticles, seems rather unlikely especially in the underdosing range. Moreover, the examination of TEM micrographs does not reveal the presence of an abundant hydroxide precipitate (See Fig. S2 in Supporting Information). A simple charge neutralization mechanism can also be argued since the electrophoretic mobility of silica aggregates is negative. However, a hetero-aggregation process involving negative silica particles attached by positive nano-size coagulant species may reconcile all the observations. In that framework, a local charge neutralization within the aggregate is sufficient to ensure the build-up of aggregates, the negative electrophoretic mobility being explained by the terminal attachment of partially neutralized and still negative silica particles in excess at the outer part of aggregates. The linear decrease in residual turbidity and the concomitant increase in aggregate size observed with increasing phosphate concentration when using an underdose of iron coagulant (Figs. 3 and 4b), are also consistent with a hetero-aggregation framework. Indeed, when mixing large and small oppositely charged particles, previous research has shown that, below the destabilization threshold, the number of hetero-aggregates obtained decreases linearly with the relative number of large and small particles (Dumont et al., 1990). In our case, a small addition of phosphate ligand determines an increase in the overall number of nanosize coagulant species, and hence promotes the growth of larger aggregates thus improving their settleability.

Although limited to less than a decade in Q, an estimate of about 1.7 for the fractal exponent of silica aggregates is consistent with a diffusion-limited cluster aggregation (DLCA) (Meakin, 1987). Such DLCA regime can be argued because the aggregates are formed in a stirred vessel. The relative importance of shear aggregation to Brownian diffusion can be assessed using the Péclet number  $Pe = 6\pi\eta Gd_0^3/kT$  in which  $\eta$  is the dynamic viscosity of the suspension ( $\eta = 1.07 \cdot 10^{-6} \text{ m}^2\text{s}^{-1}$ ),  $G$  the average velocity gradient ( $G = 135 \text{ s}^{-1}$ ),  $d_0$  the radius of silica particles ( $d_0 = 7 \text{ nm}$ ),  $k$  the Boltzmann constant and  $T$  the absolute temperature (Frappier et al., 2010). In the early stage of aggregation,  $Pe$  is about  $2 \cdot 10^{-7}$  which suggests that Brownian aggregation is largely predominant over



shear aggregation and governs the aggregate structure investigated by SAXS. For micron size aggregates, the two aggregation modes become equivalent.

The slightly higher  $D_f$  value of 1.83 obtained below a Fe/P ratio of 7 can also be explained by the same DLCA aggregation regime provided that some reorganization of aggregates is allowed (Meakin and Julien, 1988). Wu et al. (2013) have recently shown that thermal restructuring may drive an increase in the fractal dimension of DLCA aggregates that is more pronounced with a decrease in the radius of primary particles. For silica nanoparticles having a radius of 7 nm, a  $D_f$  value of about 1.9 can be expected if the bonds between primary particles are weak (Wu et al., 2013). Accordingly, this suggests that the bonds formed from the coagulant species between the silica particles are strong and even rigid above a Fe/P of 7, and that some restructuring of aggregates occurs below a Fe/P of 7 because of the slightly different nature of coagulant species that leads to a lower binding energy between the particles.

## 5. Conclusions

The aggregation of silica nanoparticles with ferric chloride was studied in the presence of small amounts of phosphate ligand. The characteristics of aggregates formed were described using a combination of techniques, i.e. laser granulometry, turbidity measurements, SAXS, TEM-EDXS microanalysis and EXAFS at the Fe K-edge. We found that the addition of phosphate dramatically modifies the nature of hydrolysis products without changing the aggregation mechanism. The phosphate ligands terminate the polymerization of Fe-octahedra chains to lead to an increasing number of Fe-oligomers bridged by phosphate tetrahedra. An elemental ratio Fe/P of about 7 appears optimal for the production of efficient positively charged coagulant species. The SAXS results indicate that the size of those coagulant species remains in the nanoscale range and reveal that a Diffusion Limited Cluster Aggregation governs the structure of aggregates in the early stage of aggregation.

The prevalence of non-equilibrium Fe–P species formed in the course of chemical coagulation of silica particles suggests that thermodynamic approaches of phosphorus removal with iron or aluminum coagulants are not of much use. Instead, the relative contents in hydrolyzing metal coagulant and in complexing anions in the raw water to be treated, coupled with a partial charge model (Jolivet, 2019), might be better suited for describing the coagulant species likely to be formed. Our results demonstrate the usefulness of coupling microscopic and spectroscopic approaches to clear up the nature of active coagulant species and to properly understand coagulation mechanism.

## Acknowledgements

Arkema is gratefully acknowledged for providing the commercial coagulant CLARFER used in the experiments. BL would like to thank Yves Auda for his advice on the statistical analyses.

## Appendix A. Supplementary data

Supplementary data to this article can be found online at <https://doi.org/10.1016/j.watres.2019.114960>.

## References

Allison, S., 2009. Electrokinetic modeling of metal oxides. *J. Colloid Interface Sci.* 332, 1–10. <https://doi.org/10.1016/j.jcis.2008.12.004>.  
Axelos, M.A.V., Tchoubar, D., Bottero, J.-Y., 1989. Small Angle X-ray Scattering investigation of the silica/water interface: evolution of the structure with pH. *Langmuir* 5, 1186–1190. <https://doi.org/10.1021/la00089a010>.

Bolt, G.H., 1957. Determination of the charge density of silica sols. *J. Phys. Chem.* 61, 1166–1169. <https://doi.org/10.1021/j150555a007>.  
Bonnin, D., Calas, G., Suquet, H., Pzerat, H., 1985. Site occupancy of  $\text{Fe}^{3+}$  in garfield nontronite: a spectroscopy study. *Phys. Chem. Miner.* 12, 55–65.  
Bottero, J.-Y., Manceau, A., Villieras, F., Tchoubar, D., 1994. Structure and mechanisms of formation of  $\text{FeOOH}(\text{Cl})$  polymers. *Langmuir* 10, 316–319. <https://doi.org/10.1021/la00013a046>.  
Caravelli, A.H., Contreras, E.M., Zaritzky, N.E., 2010. Phosphorus removal in batch systems using ferric chloride in the presence of activated sludges. *J. Hazard Mater.* 177, 199–208. <https://doi.org/10.1016/j.jhazmat.2009.12.018>.  
Chaignon, V., Lartiges, B.S., El Samrani, A., Mustin, C., 2002. Evolution of size distribution and transfer of mineral particles between flocs in activated sludges: an insight into floc exchange dynamics. *Water Res.* 36, 676–684. [https://doi.org/10.1016/S0043-1354\(01\)00266-4](https://doi.org/10.1016/S0043-1354(01)00266-4).  
Chen, W., Zheng, H., Teng, H., Wang, Y., Zhang, Y., Zhao, C., Liao, Y., 2015. Enhanced coagulation-flocculation performance of iron-based coagulants effects of  $\text{PO}_4^{3-}$  and  $\text{SiO}_2$  modifiers. *PLoS One* 10 (9), e0137116. <https://doi.org/10.1371/journal.pone.0137116>.  
Chen, K.-Y., Hsu, L.-C., Chan, Y.-T., Cho, Y.-L., Tsao, F.-Y., Tzou, Y.-M., Hsieh, Y.-C., Liu, Y.-T., 2018. Phosphate removal in relation to structural development of humic acid-iron coprecipitates. *Sci. Rep.* 8, 10363. <https://doi.org/10.1038/s41598-018-28568-7>.  
Collins, R.N., Rosso, K.M., Rose, A.L., Glover, C.J., Waite, T.D., 2016. An in situ XAS study of ferric iron hydrolysis and precipitation in the presence of perchlorate, nitrate, chloride, and sulfate. *Geochem. Cosmochim. Acta* 177, 150–169. <https://doi.org/10.1016/j.gca.2016.01.021>.  
Doelsch, E., Rose, J., Masion, A., Bottero, J.-Y., Nahon, D., Bertsch, P., 2000. Speciation and crystal chemistry of iron (III) chloride hydrolyzed in the presence of  $\text{SiO}_4$  ligands. 1. An Fe K-edge EXAFS study. *Langmuir* 16, 4726–4731. <https://doi.org/10.1021/la991378h>.  
Doelsch, E., Masion, A., Rose, J., Stone, W.E.E., Bottero, J.-Y., Bertsch, P., 2003. Chemistry and structure of colloids obtained by hydrolysis of  $\text{Fe}(\text{III})$  in the presence of  $\text{SiO}_4$  ligands. *Colloid. Surf. Physicochem. Eng. Asp.* 136, 121–128. [https://doi.org/10.1016/S0927-7757\(02\)00566-6](https://doi.org/10.1016/S0927-7757(02)00566-6).  
Duan, J.M., Gregory, J., 2003. Coagulation by hydrolyzing metal salts. *Adv. Colloid Interface Sci.* 100, 475–502. [https://doi.org/10.1016/S0001-8686\(02\)00067-2](https://doi.org/10.1016/S0001-8686(02)00067-2).  
Dumont, F., Ameryckx, G., Watillon, A., 1990. Heterocoagulation between small and large colloidal particles. Part I. Equilibrium aspects. *Colloids Surface* 51, 171–188. [https://doi.org/10.1016/0166-6622\(90\)80140-Y](https://doi.org/10.1016/0166-6622(90)80140-Y).  
El samrani, A.G., Lartiges, B.S., Montargès-Pelletier, E., Kazpard, V., Barrès, O., Ghanbaja, J., 2004. Clarification of municipal sewage with ferric chloride: the nature of coagulant species. *Water Res.* 38, 756–768. <https://doi.org/10.1016/j.watres.2003.10.002>.  
El Samrani, A.G., Ouaini, N., Lartiges, B.S., Kazpard, V., Ibriki, A., Saad, Z., 2006. Behavior of complexing ligands during coagulation-flocculation by ferric chloride: a comparative study between sewage water and an engineered colloidal model. *J. Environ. Eng. Sci.* 5, 397–404. <https://doi.org/10.1139/s06-006>.  
El Samrani, A.G., Lartiges, B.S., Villieras, F., 2008. Chemical coagulation of combined sewer overflow: heavy metal removal and treatment optimization. *Water Res.* 42, 951–960. <https://doi.org/10.1016/j.watres.2007.09.009>.  
Fatombi, J.K., Lartiges, B., Aminou, T., Barres, O., Caillet, C., 2013. A natural coagulant protein from copra (*Cocos nucifera*): Isolation, characterization, and potential for water purification. *Separ. Purif. Technol.* 116, 35–40. <https://doi.org/10.1016/j.seppur.2013.05.015>.  
Frappier, G., Lartiges, B.S., Skali-Lami, S., 2010. Floc cohesive force in reversible aggregation: a Couette laminar flow investigation. *Langmuir* 26 (13), 10475–10488. <https://doi.org/10.1021/la9046947>.  
Hauduc, H., Takacs, I., Smith, S., Szabo, A., Murthy, S., Daigger, G.T., Sperandio, M., 2015. A dynamic physicochemical model for chemical phosphorus removal. *Water Res.* 73, 157–170. <https://doi.org/10.1016/j.watres.2014.12.053>.  
Houhou, J., Lartiges, B.S., Hofmann, A., Frappier, G., Ghanbaja, J., Temgoua, A., 2009. Phosphate dynamics in an urban sewer: a case study of Nancy, France. *Water Res.* 43, 1088–1100. <https://doi.org/10.1016/j.watres.2008.11.052>.  
Jolivet, J.-P., 2019. *Metal Oxide Nanostructures Chemistry: Synthesis from Aqueous Solutions*, second ed. Oxford University Press, ISBN 9780190928117, p. 416.  
Lartiges, B.S., Bottero, J.-Y., Derrendinger, L.S., Humbert, B., Tekely, P., Sutý, H., 1997. Flocculation of colloidal silica with hydrolyzed aluminum: an  $^{27}\text{Al}$  solid state NMR investigation. *Langmuir* 13, 147–152. <https://doi.org/10.1021/la951029x>.  
Lente, G., Fabian, I., 2002. Ligand substitution kinetics of the  $\text{Fe}(\text{III})$  hydroxo dimer with simple inorganic ligands. *Inorg. Chem.* 41, 1306–1314. <https://doi.org/10.1021/ic011013w>.  
Lente, G., Magalhaes, M.E.A., Fabian, I., 2000. Kinetics and mechanism of complex formation reactions in the  $\text{Fe}(\text{III})$ -Phosphate ion system at large  $\text{Fe}(\text{III})$  excess. Formation of a tetranuclear complex. *Inorg. Chem.* 39, 1950–1954. <https://doi.org/10.1021/ic991017p>.  
Manceau, A., Calas, G., 1986. Nickel-Bearing clay minerals: II. Intracrystalline distribution of Nickel: an X-ray absorption study. *Clay Miner.* 21, 341–360. <https://doi.org/10.1180/claymin.1986.021.3.07>.  
Manceau, A., Drits, V., 1993. Local structure of ferrihydrite and ferroxidite by EXAFS spectroscopy. *Clay Miner.* 28, 165–184. <https://doi.org/10.1180/claymin.1993.028.2.01>.  
Masion, A., Vilge-Ritter, A., Rose, J., Stone, W.E.E., Teppen, B.J., Rybacki, D., Bottero, J.Y., 2000. Coagulation-flocculation of natural organic matter with Al salts: speciation and structure of the aggregates. *Environ. Sci. Technol.* 34 (15), 3242–3246. <https://doi.org/10.1021/es9911418>.

- Meakin, P., 1987. Fractal aggregates. *Adv. Colloid Interface Sci.* 28, 249–331. [https://doi.org/10.1016/0001-8686\(87\)80016-7](https://doi.org/10.1016/0001-8686(87)80016-7).
- Meakin, P., Jullien, R., 1988. The effect of restructuring on the geometry of clusters formed by diffusion-limited, ballistic, and reaction-limited cluster-cluster aggregation. *J. Chem. Phys.* 89, 246–250. <https://doi.org/10.1063/1.455517>.
- Meybeck, M., Helmer, R., 1989. The quality of rivers: from pristine stage to global pollution. *Palaeogeography, Palaeoclimatology, Palaeoecology (Global and Planetary Change Section)* 75, 283–309. [https://doi.org/10.1016/0921-8181\(89\)90007-6](https://doi.org/10.1016/0921-8181(89)90007-6).
- Murphy, P.J., Posner, A.M., Quirk, J.P., 1976. Characterization of hydrolyzed ferric ion solutions. A comparison of the effects of various anions on the solutions. *J. Colloid Interface Sci.* 56, 312–319. [https://doi.org/10.1016/0021-9797\(76\)90256-3](https://doi.org/10.1016/0021-9797(76)90256-3).
- Pham, N.A., Rose, A.L., Feitz, A.J., Waite, T.D., 2006. Kinetics of Fe(III) precipitation in aqueous solutions at pH 6.0–9.5 and 25°C. *Geochim. Cosmochim. Acta* 70, 640–650. <https://doi.org/10.1016/j.gca.2005.10.018>.
- Ramsay, J.D.F., Booth, B.O., 1983. Determination of structure in oxide sols and gels from neutron-scattering and nitrogen adsorption measurements. *J. Chem. Soc. Faraday Trans. 1* 79, 173–184. <https://doi.org/10.1039/F19837900173>.
- Rose, J., Manceau, A., Bottero, J.-Y., Masion, A., Garcia, F., 1996. Nucleation and growth mechanisms of the Fe oxyhydroxide in the presence of PO<sub>4</sub> ions. 1. Fe K-edge EXAFS study. *Langmuir* 12, 6701–6707. <https://doi.org/10.1021/la9606299>.
- Rose, J., Flank, A.-M., Masion, A., Bottero, J.-Y., Elmerich, P., 1997. Nucleation and growth mechanisms of Fe Oxyhydroxide in the presence of PO<sub>4</sub> ions. 2. P K-edge EXAFS study. *Langmuir* 13, 1827–1834. <https://doi.org/10.1021/la961039d>.
- Sieliechi, J.-M., Lartiges, B.S., Kayem, G.J., Hupont, S., Frochot, C., Thieme, J., Ghanbaja, J., d'Espinose de la Caillerie, J.-B., Barrès, O., Kamga, R., Levitz, P., Michot, L.J., 2008. Changes in humic acid conformation during coagulation with ferric chloride: implications for drinking water treatment. *Water Res.* 42, 2111–2123. <https://doi.org/10.1016/j.watres.2007.11.017>.
- Sieliechi, J., Lartiges, B., Skali-Lami, S., Kayem, J., Kamga, R., 2016. Floc compaction during ballasted aggregation. *Water Res.* 105, 361–369. <https://doi.org/10.1016/j.watres.2016.09.015>.
- Smith, S., Takacs, I., Murthy, S., Daigger, G.T., Szabo, A., 2008. Phosphate complexation model and its implications for chemical phosphorus removal. *Water Environ. Res.* 80 (5), 428–438.
- Tchoubar, D., Bottero, J.-Y., Quienne, P., Arnaud, M., 1991. Partial hydrolysis of ferric chloride salt. Structural investigation by photon –correlation spectroscopy and small-angle X-ray scattering. *Langmuir* 7, 398–402. <https://doi.org/10.1021/la00050a034>.
- Vilgé-Ritter, A., Rose, J., Masion, A., Bottero, J.-Y., Lainé, J.-M., 1999. Chemistry and structure of aggregates formed with Fe-Salts and natural organic matter. *Colloid. Surf. Physicochem. Eng. Asp.* 297–308. [https://doi.org/10.1016/S0927-7757\(98\)00325-2](https://doi.org/10.1016/S0927-7757(98)00325-2).
- Wang, D.S., Tang, H.X., Cao, F.C., 2000. Particle speciation analysis of inorganic polymer flocculants: an examination by photon correlation spectroscopy. *Colloid. Surf. Physicochem. Eng. Asp.* 166, 27–32. [https://doi.org/10.1016/S0927-7757\(99\)00420-3](https://doi.org/10.1016/S0927-7757(99)00420-3).
- Wu, H., Lattuada, M., Morbidelli, M., 2013. Dependence of fractal dimension of DLCA clusters on size of primary particles. *Adv. Colloid Interface Sci.* 195–196, 41–49. <https://doi.org/10.1016/j.cis.2013.04.001>.
- Yu, W., Gregory, J., Campos, L.C., Graham, N., 2015. Dependence of floc properties on coagulant type, dosing mode and nature of particles. *Water Res.* 68, 119–126. <https://doi.org/10.1016/j.watres.2014.09.045>.
- Zhang, H., Waychunas, G.A., Banfield, J.F., 2015. Molecular dynamics simulation study of the early stages of iron oxyhydroxide nanoparticles in aqueous solutions. *J. Phys. Chem. B* 119, 10630–10642. <https://doi.org/10.1021/acs.jpcc.5b03801>.
- Zhu, M., Legg, B., Zhang, H., Gilbert, B., Ren, Y., Banfield, J.F., Waychunas, G.A., 2012. Early stage formation of Iron oxyhydroxides during Neutralization of simulated acid mine drainage solutions. *Environ. Sci. Technol.* 46 (15), 8140–8147. <https://doi.org/10.1021/es301268g>.
- Zhu, M., Puls, B.W., Frandsen, C., Kubicki, J.D., Zhang, H., Waychunas, G.A., 2013. In situ structural characterization of ferric iron dimers in aqueous solutions: Identification of  $\mu$ -Oxo species. *Inorg. Chem.* 52, 6788–6797. <https://doi.org/10.1021/ic302053w>.
- Zhuravlev, L.T., 2000. The surface chemistry of amorphous silica. *Zhuravlev Model. Colloids and Surfaces A: Physicochemical and Engineering Aspects* 173, 1–38. [https://doi.org/10.1016/S0927-7757\(00\)00556-2](https://doi.org/10.1016/S0927-7757(00)00556-2).